ACS OMEGA

Open Access

http://pubs.acs.org/journal/acsodf

Article

Facile Synthesis of 3D NC-rGO@Ni-Foam Nanonetwork as a Binder-Free Hybrid Electrode Material for Ultrahigh Capacitance Applications

Wen Sun, Mehmet Ozdogan, Nuri Oncel, and Julia Xiaojun Zhao*

Cite This: *ACS Omega* 2025, 10, 16457−16471

Read Online

ACCESS | Metrics & More | Article Recommendations

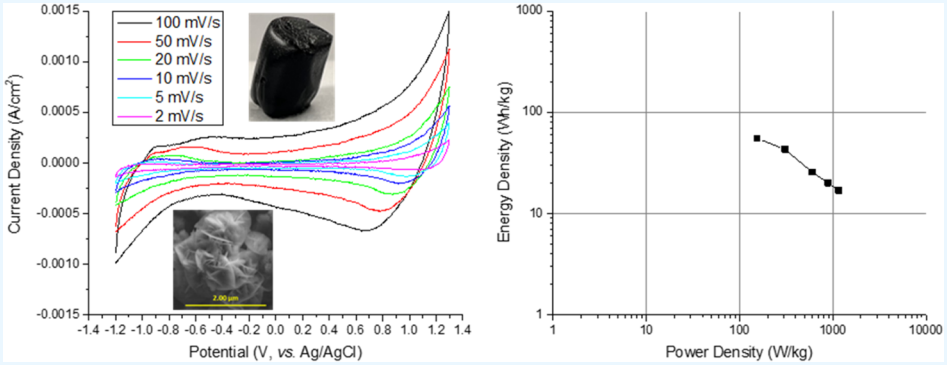

ABSTRACT: In this study, a three-dimensional (3D) structured nanomaterial has been developed to enhance the electrochemical properties of supercapacitors. The nanomaterial's structure was engineered by incorporating divalent metal ions (M^{2+}: Ni^{2+} and Co^{2+}) into reduced graphene oxide (rGO) layers supported on nickel foam (3D NC-rGO@Ni-foam), forming a binder-free hybrid electrode. This was accomplished through a combination of in situ wet-chemistry and hydrothermal techniques. This binder-free electrode material has stacked layers of rGO, which improve conductivity, while the M^{2+} ions intercalated between these layers function as redox couples, thereby significantly improving the specific capacitance. Furthermore, the Ni-foam substrate offers a porous configuration and works as the current collector. In contrast to traditional slurry coating methods, the in situ growth of nanostructures on Ni-foam is expected to enhance strong adhesion, high conductivity, and effective ion transport. The structural morphology, chemical composition, and electrochemical behavior of the 3D NC-rGO@Ni-foam electrode were comprehensively investigated using techniques such as scanning electron microscope (SEM), energy-dispersive X-ray spectroscopy (EDS), cyclic voltammetry (CV), galvanostatic charge−discharge (GCD), electrochemical impedance spectroscopy (EIS), and other analytical methods. This binder-free 3D hybrid electrode material demonstrated a specific capacitance (C_s) of 2612 F/g at 1 A/g. The symmetric device fabricated also demonstrated a substantial energy density (E) of 55 W·h/kg and a power density (P) of 155 W/kg across a wide potential window of 2.5 V. The electrochemical characteristics and mechanical stability of 3D NC-rGO@Ni-foam indicate its potential as a high-performance electrode material for scalable energy storage systems.

1. INTRODUCTION

The increasing global demand for developing alternative renewable and sustainable energy sources is primarily driven by concerns about the potential exhaustion of nonrenewable fossil fuels and the environmental impacts associated with greenhouse gas emissions.[1−3] Supercapacitors (SCs), also known as electrochemical capacitors, have garnered significant attention among various energy storage devices due to their environmental friendliness, ability to safely provide high power, rapid charging capabilities with an exceptionally long cycle life (>100,000 cycles), lightweight nature, and suitability for flexible, portable energy storage devices.[4−8] Typically comprising two electrodes, a separator, an electrolyte, and a current collector, SCs rely heavily on the electrodes, making their material composition, especially in terms of conductivity and active surface areas, of utmost importance.[9−12]

SCs can be classified according to their charge-storage mechanisms into two main types. One is called electrical double-layer capacitors (EDLCs), which store energy through

Received: December 4, 2024
Revised: March 7, 2025
Accepted: April 2, 2025
Published: April 16, 2025

https://doi.org/10.1021/acsomega.4c10988
ACS Omega 2025, 10, 16457−16471

the formation of an electric double layer at the electrode/electrolyte interface. The other type is called pseudocapacitors (PCs), which store energy through faradaic redox reactions. Additionally, the combination of these mechanisms results in hybrid capacitors.[9,13,14] EDLCs accumulate electrostatic charge at the electrode surface. Therefore, the capacitance is determined by the amount of charge, which is affected by the electrode materials' surface areas and porous structure. Carbon-based materials, such as graphene-based materials, are frequently utilized as electrodes in EDLCs due to their large specific surface area, high electrical conductivity, thermal and chemical stability, low cost, and well-established fabrication methods.[2,15−19] Among carbon-based materials, graphene stands out as a promising candidate owing to its high theoretical specific area, excellent conductivity, chemical and thermal stability, extended potential window, and remarkable mechanical flexibility. However, the practical applications of pure graphene are constrained by its low electroactive surface area, stemming from its chemically inert and hydrophobic nature.[20−22] As a result, graphene-based materials, including graphene oxide (GO) and reduced graphene oxide (rGO), have attracted significant interest in recent years. The presence of functional groups, such as carboxyl (−COOH), epoxy (−O−), carbonyl (−C═O), and hydroxyl (−OH), on GO and rGO offers active sites for additional chemical modifications, making them suitable conductive supports for nanoparticles to form nanocomposites.[15,23,24]

The capacitance of PCs typically exceeds that of pure EDLCs by about ten times, primarily due to surface faradaic reactions during the charge-storage process.[25] PCs commonly utilize metal oxides, conducting polymers, or their composites as electrode materials. However, the low electrical conductivity, insufficient utilization of transition metal oxides, and the poor cycling stability of conducting polymers contribute to unfavorable rate performances and power density.[25−28] Different from EDLCs and PCs, hybrid capacitors use composite materials combining capacitive (graphene-based) materials and redox-type (metal oxides or conducting polymers) in one paradigm which has been recognized as an effective strategy to enhance the specific capacitance (C_s) of graphene-based materials and provide high energy density (E) and power density (P).[4,11,15,29−31] The hybrid material with the best C_s of 2682.6 F/g at 1 A/g, was synthesized using the hydrothermal method by applying cobalt acetate tetrahydrate and nickel acetate tetrahydrate as metal precursors and urea as reducing agent and adjusted pH. The hybrid electrode materials ($NiCo_2O_4$/rGO/NF) were fabricated without the use of any binder materials to eliminate "dead surfaces," thereby enabling the synergistic interaction between graphene and $NiCo_2O_4$ to be fully utilized.[32] Another hybrid nanocomposite of $NiCo_2O^4$@rGO using nickel nitrate and cobalt nitrate as the metal precursors and KOH to precipitate out the metal hydroxides, followed by using hydrazine hydrate for graphene oxide reduction reaction. The C_s was 787.17 C/g at 1.0 A/g for a 3-electrode setup. A complete functional cell with the configuration NiCo2O4@rGO//Activated Carbon (AC) demonstrates high E and P at 46.01 Wh/kg and 936.69 W/kg at 10 A/g, and 25.12 Wh/kg and 2810.08 W/kg at 30 A/g, respectively.[33]

Transition metal oxides (TMOs) are promising materials for PCs due to their high theoretical C_s and numerous oxidation states, resulting in favorable redox behavior. Within the realm of TMOs, attention is drawn toward metal oxides containing different cations, as they exhibit improved redox behavior and enhanced electrical conductivity, possibly attributed to the bonding between different metal cations.[13] In mixed metal oxides, nickel cobalt oxides are particularly noteworthy due to their cost-effectiveness, natural abundance, excellent electrochemical activity, higher theoretical capacitance compared to nickel oxide and cobalt oxide respectively, and diverse nanostructures such as hierarchical flowers,[34] nanorods and nanoneedles,[35] mesoporous nanoplates,[36] nanosheets,[37−39] and nanonets/nanoflakes,[40] etc. Using a chemical method, Poonam Siwatch et al. have fabricated nanocomposite films comprising reduced graphene oxide and nickel cobalt oxides quantum dots (NCO-QDs). Different nanocomposite films were synthesized by adjusting the ratio of NCO-QDs and rGO. The C_s value of the NCO_5-$rGO_{1.5}$ was 265 F/g at 0.73 A/g, significantly higher than rGO alone (96 F/g at 0.33 A/g). The assembled ASSCs utilizing these materials exhibited a C_s value of 131 F/g at an E of 47 Wh/kg and a P of 631 W/kg, operating in a wide potential range of 1.6 V.[13]

This study employed an in situ growing technique to produce reduced graphene oxide (rGO) integrated with divalent transition metal ions (M^{2+}), specifically Ni^{2+} and Co^{2+}, on nickel foam (Ni-foam) through a one-step hydrothermal procedure. This technique can produce a three-dimensional binder-free electrode material called 3D NC-rGO@Ni-foam. This binder-free electrode material has stacked layers of reduced graphene oxide (rGO), which improves conductivity, while the M^{2+} ions intercalated between these layers[41,42] function as redox couples, significantly improving the specific capacitance (C_s). Furthermore, the Ni-foam substrate offers a porous configuration, enhancing active surface areas. The in situ synthesis of nanostructures on Ni-foam is expected to improve adhesion, conductivity, and ion transport efficiency relative to traditional slurry coating methods.[14] The electrochemical analysis of the 3D NC-rGO@Ni-foam electrode material demonstrated elevated capacitance and energy density, positioning it as a promising contender for advanced electrode materials in scalable energy storage systems.

2. EXPERIMENTAL DETAILS

2.1. Materials and Instruments. A single-layer graphene oxide (GO) aqueous solution with a concentration of 5.0 mg/mL was acquired from ACS Materials. Nickel(II) chloride hexahydrate ($NiCl_2{\cdot}6H_2O$, 98%) and cobalt(II) chloride hexahydrate ($CoCl_2{\cdot}6H_2O$, 98%) were purchased from Thermo Scientific. Potassium hydroxide (KOH, 99.98%, trace metal basis) pellets were purchased from Thermo Scientific Chemicals. Ethanol (200 Proof, undenatured) was purchased from Decon Laboratories Inc. The Ni-foam was purchased from MTI Corporation. All chemical reagents were used without further purification. Deionized (DI) water, with a resistivity of 18.2 MΩ·cm, was obtained using a Millipore water purification system.

A vacuum oven (VWR International West Chester, PA) was used for hydrothermal. The morphology of the nanocomposite was examined using a Hitachi SU8010 field emission scanning electron microscope (FE-SEM) from Hitachi, Japan. Elemental analysis was conducted using an energy-dispersive X-ray spectroscopy (EDS) (Oxford, X-Max) integrated into the SEM. A stirring plate (205 Auto Stirrer, VWR Scientific Products) was used to help dissolve the metal precursors. A sonicator from Branson, Buffalo Grove, IL, was utilized to

https://doi.org/10.1021/acsomega.4c10988
ACS Omega 2025, 10, 16457−16471

Scheme 1. Schematic Representation of a Binder-Free 3D NC-rGO Cylinder Synthesis Using a One-Step Hydrothermal Process

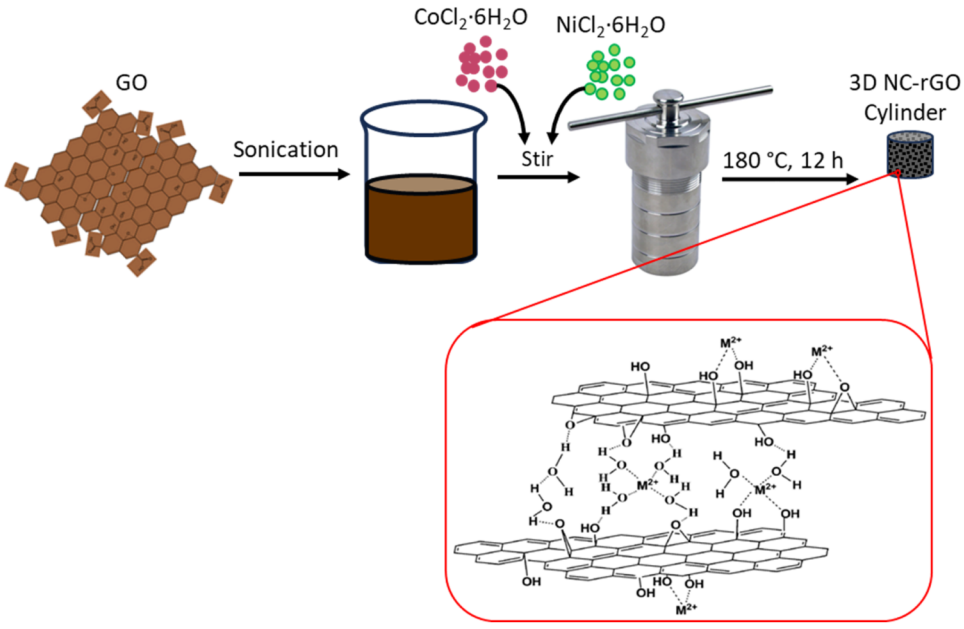

ensure the uniform dispersion of GO in deionized (DI) water. The surface area and porosity were analyzed using the Brunauer−Emmet−Teller (BET) method with a Micromeritics ASAP 2020 Plus Physisorption Analyzer. The samples underwent automatic degassing before measurement. The nanocomposite's X-ray diffraction (XRD) pattern was obtained using a Rigaku SmartLab X-ray diffractometer. To analyze the functional groups, UV−vis absorption spectra were recorded with a Lambda 1050 UV/vis/NIR spectrometer (PerkinElmer, Santa Clara, CA). X-ray photoelectron spectroscopy (XPS) experiments were carried out using a PHI-5400 XPS system, with Si wafers serving as substrates. The nanocomposite's metal loading was measured through inductively coupled plasma mass spectrometry (iCAP Qc ICP-MS, ThermoFisher Scientific). The potentiostat (Framework version 7.8.2, Reference 600, Gamry Instruments) was used for all the electrochemical examinations.

2.2. Synthesis of 3D NC-rGO@Ni-Foam. To create the 3D NC-rGO@Ni-foam, start by dispersing GO (2 mg/mL) in DI water and sonicating it for 30 min. Next, stir in metal precursors (1 wt % of $NiCl_2·6H_2O$ and $CoCl_2·6H_2O$) for 3 h. Transfer this mixture to a 20 mL Teflon-lined autoclave and heat it to 180 °C for 12 h. After cooling to room temperature, a black 3D NC-rGO cylinder will be produced.

Before synthesizing the 3D NC-rGO@Ni-foam, the Ni-foam underwent a preparation process. Initially, it was immersed in acetone and subjected to 15 min of sonication, followed by immersion in a 3.0 mol/L HCl and another 15 min sonication to eliminate the surface oxide layer. Subsequently, the pretreated Ni-foam underwent multiple washes with ethanol and DI water before being dried in an oven for 2 h.

The synthesis of the 3D NC-rGO@Ni-foam followed the same hydrothermal method used to prepare the 3D NC-rGO cylinder. Initially, GO was dispersed in DI water at a concentration of 2 mg/mL and underwent sonication for 30 min. Subsequently, the metal precursors, comprising a total of 1 wt % $NiCl_2·6H_2O$ and $CoCl_2·6H_2O$ were added to the GO dispersion and stirred for 3 h. The mixture was then transferred into a 20 mL Teflon-lined autoclave with a piece of flexible Ni-foam (50 mm × 10 mm × 1 mm) and then heated at 180 °C. After a reaction time of 12 h, the autoclave was allowed to cool to room temperature. The resulting product, the 3D NC-rGO@Ni-foam, was then dried overnight. The total mass loading for the NC-rGO nanonetwork was around 3.0 ± 0.1 mg per 1 cm × 1 cm Ni-foam.

2.3. Electrochemical Examinations. *2.3.1. Preparation of Electrochemical Testing Systems.* The electrochemical characteristics of the 3D NC-rGO@Ni-foam were analyzed using a potentiostat from Gamry. Two types of testing cells are used to assess the electrode performance of supercapacitors. The first is the 3-electrode cell, consisting of a working electrode (WE), counter electrode (CE), and reference electrode (RE). This configuration is widely employed for evaluating single-electrode performance. In this system, an Ag/AgCl (sat. KCl) reference electrode pairs with a platinum mesh cylinder as the counter electrode. The second type is the Swagelok cell, which features a separator placed between two working electrodes. This design is utilized to gauge the performance of supercapacitors, yielding reliable parameters such as energy density, power density, and cell cycling life, along with potential applications.

2.3.2. Electrochemical Measurements. A range of electrochemical tests, including cyclic voltammetry (CV), galvanostatic charge−discharge (GCD), and electrochemical impedance spectroscopy (EIS), were conducted with a 2 M KOH electrolyte. The section on electrochemical examination results provides a complete description of these tests. GCD tests were carried out at different current densities ranging from 3 to 20 mA/cm^2, while CV was performed at various scan rates from 2 to 100 mV/s. EIS measurements were conducted under a frequency range of 0.01 Hz to 100 kHz. The self-discharge was measured during a 2 h hold at a fixed cell potential, and thereafter, the cell self-discharge profile was recorded at an open circuit for 24 h. The internal resistance (iR) drop was calculated by subtracting the discharge voltage drop, obtained from the GCD plots, from the total voltage.

https://doi.org/10.1021/acsomega.4c10988
ACS Omega 2025, 10, 16457−16471

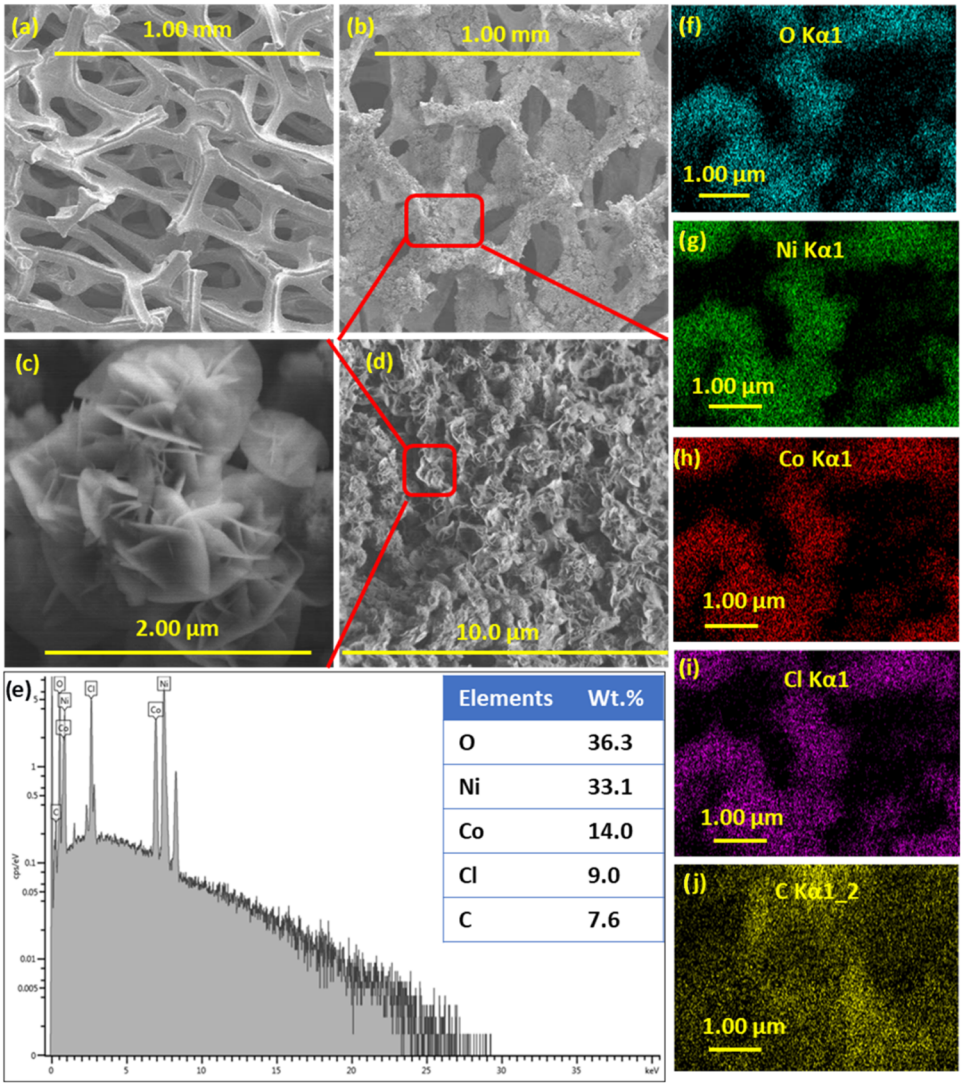

Figure 1. (a) Shows an SEM image of cleaned bare Ni-foam. (b) Shows an SEM image of the 3D NC-rGO@Ni-foam. (c, d) are SEM images of the 3D NC-rGO with a flower-like morphology. (e) Shows the EDS analysis of O, Ni, Co, Cl, and C elements. (f–j) The EDS elemental maps of O, Ni, Co, Cl, and C elements.

3. RESULTS AND DISCUSSION

3.1. Design of the 3D NC-rGO@Ni-Foam. The Fabrication of 3D NC-rGO was achieved through a one-step hydrothermal method inspired by previous works by Jiang and Miao.[41,42] Jiang's study revealed a gel-like 3D rGO structure created by linking rGO sheets with divalent ions (like Ca^{2+}, Ni^{2+}, or Co^{2+}) and water molecules through hydrothermal treatment. In this structure, the rGO sheets serve as the skeleton, while the water molecules and divalent metal ions function as the filler and linker, respectively. The resulting gel-like structure mainly consisted of single or double layers of rGO isolated by interlamellar water molecules. Subsequent freeze-drying facilitated the formation of a dried 3D rGO structure with micropores, aided by introducing poly(vinyl alcohol) as a strengthening agent.[41] Miao's study employed a hydrothermal method to create graphene nanosheets (approximately 10 nm) arranged into three-dimensional porous structures uniformly applied to Ni-foam, resulting in the NF/G substrate. When KOH was added at low concentrations of GO, it facilitated the formation of flower-like Ni−Co−S nanosheets on the NF/G substrate through electrodeposition, creating the NF/G/Ni−Co−S composite. The three-dimensional graphene architecture enhanced the efficient use of electroactive species and improved reaction conditions kinetics.[42]

In our work, illustrated in Scheme 1, we utilized two transition metal cations (Ni^{2+} and Co^{2+}) as linkers to integrate into the layers of rGO to enhance redox behavior and electrical conductivity via interactions among various metal cations. In this schematic diagram, GO (2 mg/mL) was distributed in deionized water and subjected to sonication for 30 min. Subsequently, two metal precursors (1 wt % of $NiCl_2{\cdot}6H_2O$ and $CoCl_2{\cdot}6H_2O$) were included and agitated for 3 h. The mixture was then transferred to a 20 mL Teflon-lined autoclave and heated to 180 °C for 12 h. Upon cooling to room temperature, a black 3D NC-rGO cylinder was formed.

3.2. Characterizations of the 3D NC-rGO@Ni-Foam. *3.2.1. Morphology and Composition of the 3D NC-rGO@Ni-Foam.* The surface morphology and structure of the 3D NC-rGO@Ni-foam were investigated using SEM. In Figure 1a, the SEM image displays the cleaned bare Ni-foam with a notably porous structure. When compared to the cleaned bare Ni-

https://doi.org/10.1021/acsomega.4c10988
ACS Omega 2025, 10, 16457−16471

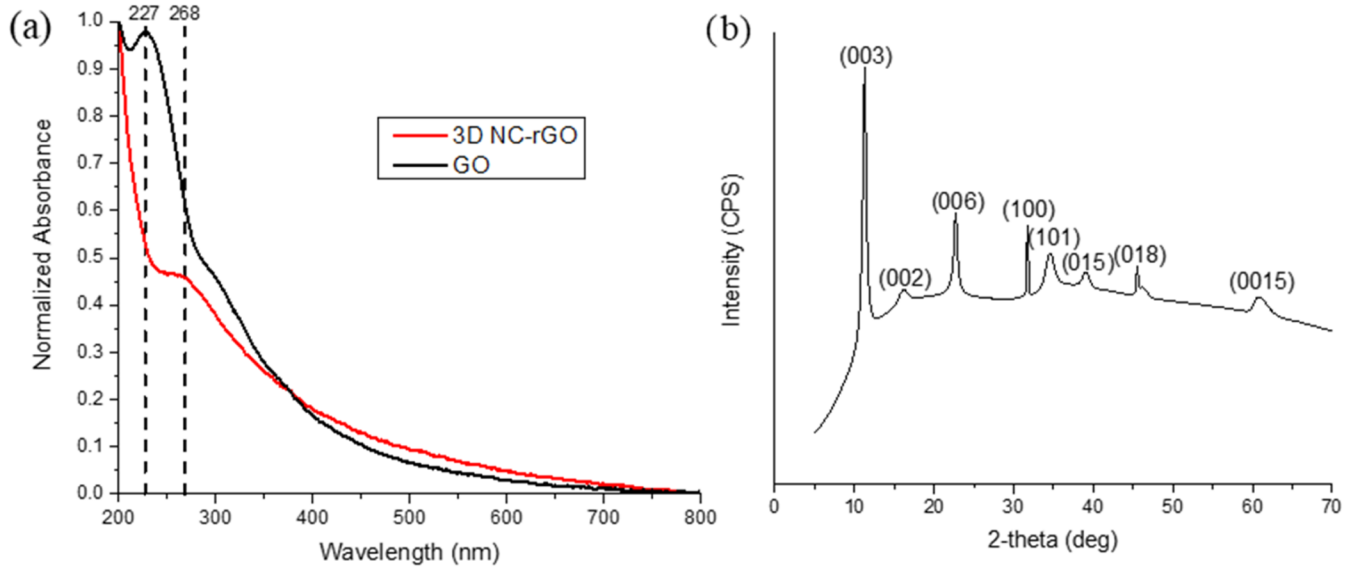

Figure 2. (a) UV−vis absorption spectra of GO and 3D NC-rGO. (b) XRD pattern of 3D NC-rGO.

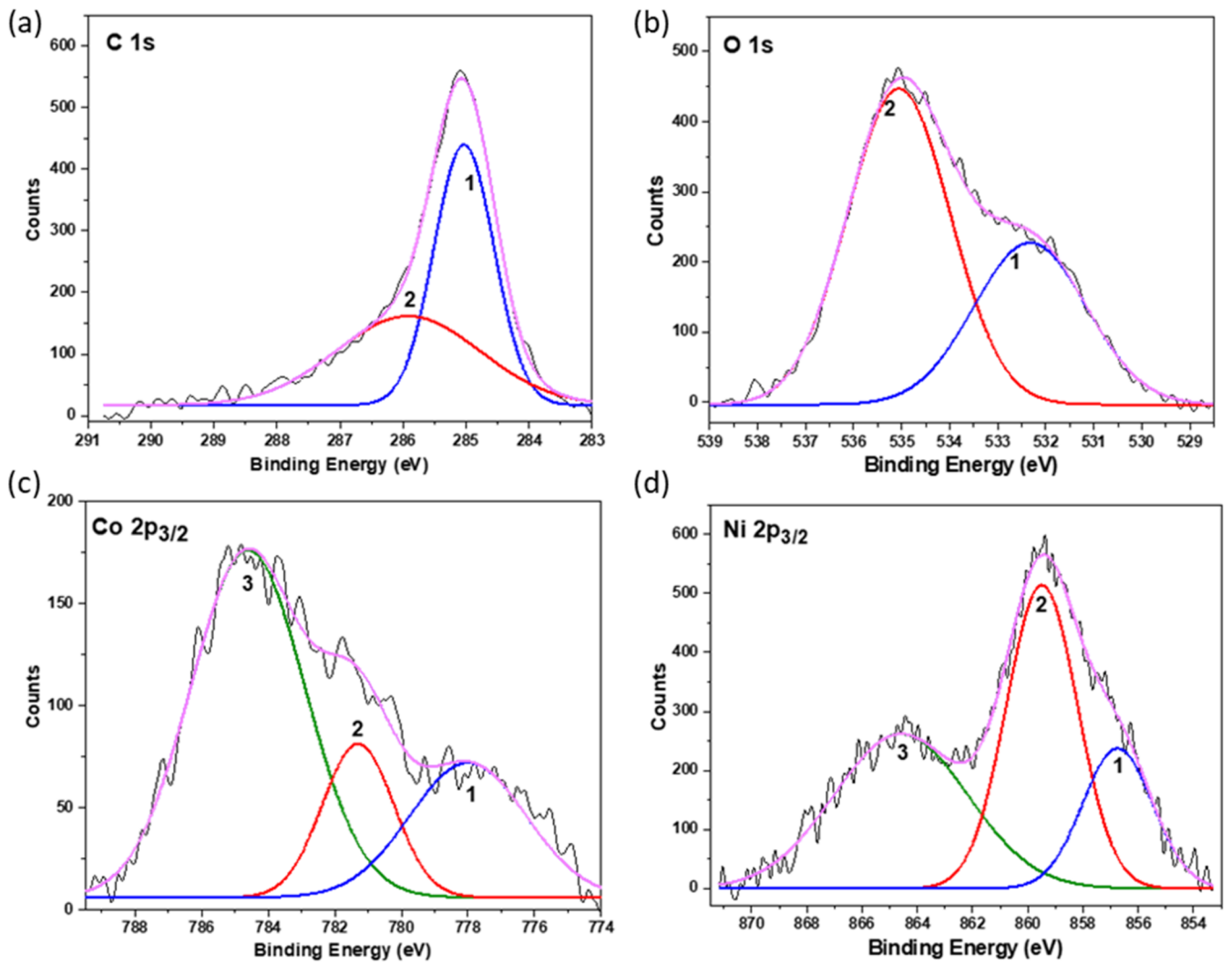

Figure 3. High-resolution XPS spectra of C 1s (a), O 1s (b), Co $2p_{3/2}$ (c), and Ni $2p_{3/2}$ (d) regions for the 3D NC-rGO.

foam, the 3D NC-rGO@Ni-foam also exhibits a porous structure, as depicted in Figure 1b, albeit with smaller pores due to the material covering the Ni-foam. The porous structure of the Ni-foam allows electrolyte ions to diffuse easily,

https://doi.org/10.1021/acsomega.4c10988
ACS Omega 2025, 10, 16457−16471

enhancing ion transport and accelerating charge−discharge rates on the electrode. Figure 1c,1d show SEM images of the 3D NC-rGO, revealing a flower-like structure that contributes to an enlarged surface area, enhancing the material's capacitance characteristics. To validate this observation further, the BET method was used to measure the specific surface area and porosity of Ni-foam and NC-rGO@Ni-foam. The BET surface area of Ni-foam was measured at 0.41 m^2/g, which is significantly lower than that of NC-rGO@Ni-foam, exhibiting a BET surface area of 7.76 m^2/g and a Langmuir surface area of 10.71 m^2/g, indicating a much higher electrochemically active surface. Additionally, the pore volume of NC-rGO@NI-foam (0.0038 cm^3/g) was markedly greater than that of Ni Foam (0.00012 cm^3/g), demonstrating an enhanced capacity for ion adsorption and transport. The average pore diameter of NC-rGO@Ni-foam, ranging from 1.94 nm (BET method) to 2.26 nm (D-H adsorption method), falls within the mesoporous range, which is ideal for efficient electrolyte ion diffusion in supercapacitor applications. In contrast, Ni-foam exhibited negligible microporosity, making it unsuitable as an active electrode material, though it remains effective as a conductive current collector. The higher surface area, larger pore volume, and optimized mesoporosity of NC-rGO@Ni-foam make it a promising candidate for high-performance supercapacitors, offering enhanced charge storage capacity and improved ion transport efficiency.

An EDS analysis was conducted to examine the elemental composition of the 3D NC-rGO. As illustrated in the EDS spectrum in Figure 1e, O, Ni, Co, Cl, and C were detected. Ni, Co, and partially O are associated with the formation of transition metal oxides in the sample, while C and partially O correspond to the rGO formation. The presence of Cl is attributed to the metal precursors added during the synthetic process. The EDS mapping function delineates individual elements in Figure 1f−j, confirming the homogeneous distribution of Ni, Co, C, and O elements in the prepared sample. The 3D NC-rGO showed an average Ni content of 29.4 wt % and Co loading of 8.37 wt %, as determined by ICP-MS after nitric acid microwave digestion. The reasons that caused differences between EDS and ICP-MS results of weight percentage of metals are (1) EDS analysis scanned the surface of the sample, but ICP-MS analysis was based on the bulk material. (2) The EDS sample is NC-rGO@Ni-foam, but the ICP-MS sample is without Ni-foam.

3.2.2. Functional Groups of the 3D NC-rGO@Ni-Foam. Three spectroscopic characterizations were performed to validate further the desired functional groups on the synthesized 3D NC-rGO@Ni-foam, including UV−vis spectra, XPS, and XRD. Figure 2a presents the UV−vis spectra of GO and the 3D NC-rGO. The pure GO shows an absorption peak at 227 nm (black curve). Following the 12 h hydrothermal process, the peak shifts to 268 nm (red curve), indicating the successful reduction of GO to rGO. The crystal structure of 3D NC-rGO was investigated using powder XRD, as shown in Figure 2b. Based on the database references, the diffraction peaks at 2θ angles of 11.3, 22.7, 34.6, 39.0, 46.2, and 60.7° correspond to (0,0,3), (0,0,6), (1,0,1), (0,1,5), (0,1,8), (0,0,15) planes of jamborite crystal (H_2NiO_2). Additionally, diffraction peaks at 2θ angles of 16.1, 39.0, 46.2, and 60.7° are associated with the (0,0,2), (2,0,-2), (2,0,-4), and (1,1,5) planes of cobalt dioxide. Peaks observed at 31.7, 34.6, 45.5, and 60.7° correspond to the (1,0,0), (1,0,1), (1,0,2), and (1,0,3) planes of nickel oxide. These assignments were made based on standard database values.

XPS analysis confirmed the elemental composition and chemical states of the 3D NC-rGO@Ni-foam, as shown in Figure 3 and detailed in Table 1. The substrate was cleaned

Table 1. Binding Energies for O, C, Co, and Ni Spectra

elements	peaks	binding energy (eV)	speciation
O	(1) O 1s	532.3	hydroxide
	(2) O 1s	535.1	weakly adsorbed surface species
C	(1) C 1s	285.0	C═C
	(2) C 1s	286.0	C−O
Co	(1) Co $2p_{3/2}$	778.0	Co metal
	(2) Co $2p_{3/2}$	781.3	$Co(OH)_2$ + $CoCl_2$
	(3) Co $2p_{3/2}$	784.6	multiplet splitting
Ni	(1) Ni $2p_{3/2}$	856.8	$Ni(OH)_2$ + $NiCl_2$
	(2) Ni $2p_{3/2}$	859.5	multiplet splitting
	(3) Ni $2p_{3/2}$	864.6	satellite feature

before dispersing the 3D NC-rGO sample onto the Si/SiO_2 substrate. This process involved ultrasonic cleaning baths in acetone, isopropanol alcohol, and distilled water sequentially. Subsequently, the substrate was air-dried to eliminate any residual solvents. The 3D NC-rGO sample was then dispersed onto the prepared Si/SiO_2 substrate and placed in a desiccator. The sample was left to dry overnight under vacuum conditions.

XPS analysis was performed using a PHI-5400 XPS system, operated under an ultrahigh vacuum with a base pressure of 2×10^{-10} mbar. The analysis utilized a nonmonochromatized Al Kα X-ray source, emitting photons with an energy of 1486.6 eV. Initial survey scans were conducted at a pass energy of 89.45 eV, employing a step size of 0.500 eV. These scans provided a broad overview of the chemical composition on the surface of the 3D NC-rGO sample. For detailed analysis, high-resolution scans were carried out at a pass energy of 17.9 eV with a finer step size of 0.025 eV. The collected high-resolution spectra were analyzed using Shirley-type background subtraction and Gaussian peak fitting using Origin Graphing and Analysis software.

The comprehensive survey scan, ranging from 0 to 1400 eV, identified prominent peaks corresponding to C 1s, O 1s, Ni 2p, Cl 2p, and Co 2p regions. A high-resolution scan of the C 1s region indicated the presence of two fitted components at 285.0 and 286.0 eV. These components are attributed to carbon atoms involved in single and double carbon bonds (C−C and C═C) and single carbon−oxygen bonds (C−O), respectively. The presence of these peaks highlights the characteristic graphene structure, while the absence of other oxygen-related functional group peaks (C═O and O−C═O) indicates the effective reduction of graphene oxide.[23] The in-depth analysis of the Ni $2p_{3/2}$ and Co $2p_{3/2}$ spectral regions revealed that the binding energies of both elements shifted to higher binding energies, 856.8 eV (an increase of +3.8 eV), and 781.3 eV (an increase of +3.1 eV) respectively. These high binding energies are indicative of the formation of metal hydroxides and halides. The observed shifts toward higher binding energies are consistent with the formation of $Co(OH)_2$ and $Ni(OH)_2$, suggesting the predominance of these hydroxide states in the sample. The absence of peaks associated with metal oxides in the O 1s region supports this assignment, reinforcing the conclusion that the material

https://doi.org/10.1021/acsomega.4c10988
ACS Omega 2025, 10, 16457−16471

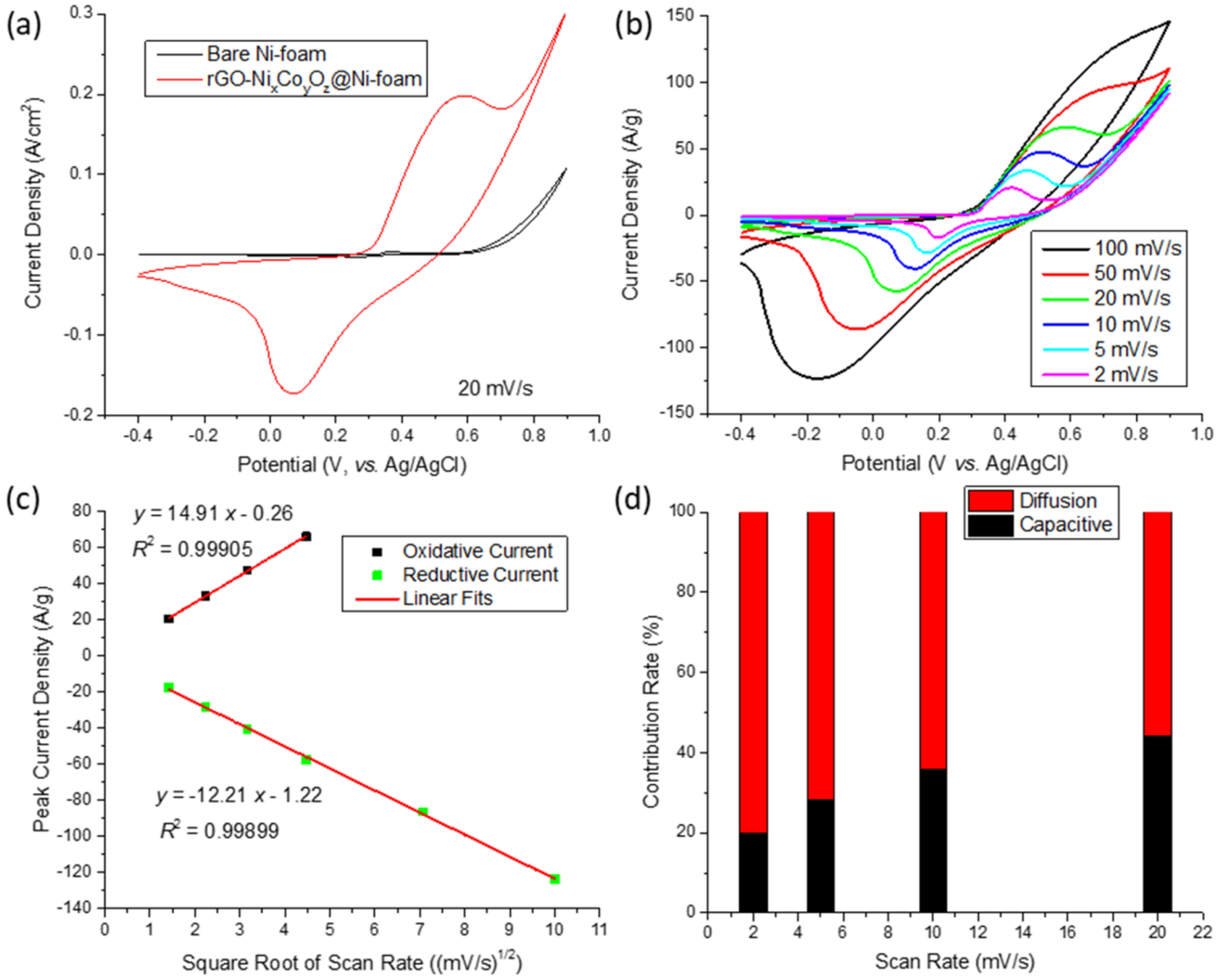

Figure 4. (a) Cleaned Ni-foam CV curve and the 3D NC-rGO@Ni-foam electrode CV curve at 20 mV/s scan rate in a potential window between −0.4 to 0.9 V. (b) CV curves of the 3D NC-rGO@Ni-foam electrode at various scan rates under a potential range between −0.4 to 0.9 V. (c) Linear fits of the square root of scan rates vs peak current densities. (d) Deconvoluted percentages of diffusive and capacitive currents were attained using Dunn's method.

predominantly features Co^{2+} and Ni^{2+} ions in the hydroxide form. This evidence is crucial for confirming the presence of divalent ion linkages.[43] However, the presence of Cl 2p peak in the survey, albeit small, suggests the presence of $CoCl_2$ and $NiCl_2$ besides metal hydroxides. The analysis also suggests retaining a certain amount of Co in its metallic state. Observations of multiplet splitting effects in the Ni and Co $2p_{3/2}$ levels and satellite feature in Ni $2p_{3/2}$ highlight the presence of unpaired electrons in the valence band, resulting in multiple peak natures, underscoring the complex electronic structure of the Ni and Co species in the sample.[44,45] The analysis of the O 1s peak further supported the presence of hydroxide groups on the surface, aligning with the expected chemical composition for Ni and Co species. This observation agrees with previously published work confirming the hydroxide nature of the surface groups.[44]

3.3. Electrochemical Examination Results. This section outlines the specifics of CV, GCD, EIS, charge storage mechanisms, potential window, iR drops, specific capacitances, energy density, power density, cycling life, cycling stability, and resistance properties. CV is a potentiodynamic electrochemical measurement where a linear electric potential is applied between the cathode and anode in a Swagelok cell, and between the working electrode (WE) and reference electrode (RE) in a 3-electrode cell. The scan rate represents the linear change in electric potential, while the potential range is influenced by the electrode materials, electrolyte, and test cell configuration. CV curves aid in determining capacitances, potential windows, and cycling life for electrodes. Typically, CV curves for Electric double-layer capacitor (EDLC) materials are rectangular, whereas those for Pseudocapacitor (PC) materials usually display pairs of redox peaks. Notably, if a material exhibits both EDLC and PC behaviors, CV curves can differentiate the capacitance contributions of these two mechanisms; EDLC response current correlates directly with the scan rate, while pseudocapacitance correlates with the square root of the scan rate mechanism.[9,46,47] GCD represents another measurement method that involves repeatedly charging and discharging at a constant current until the voltage reaches the specified set point. It requires selecting an appropriate current level to ensure GCD data is consistent and comparable. The charge/discharge profile typically shows a

https://doi.org/10.1021/acsomega.4c10988
ACS Omega 2025, 10, 16457−16471

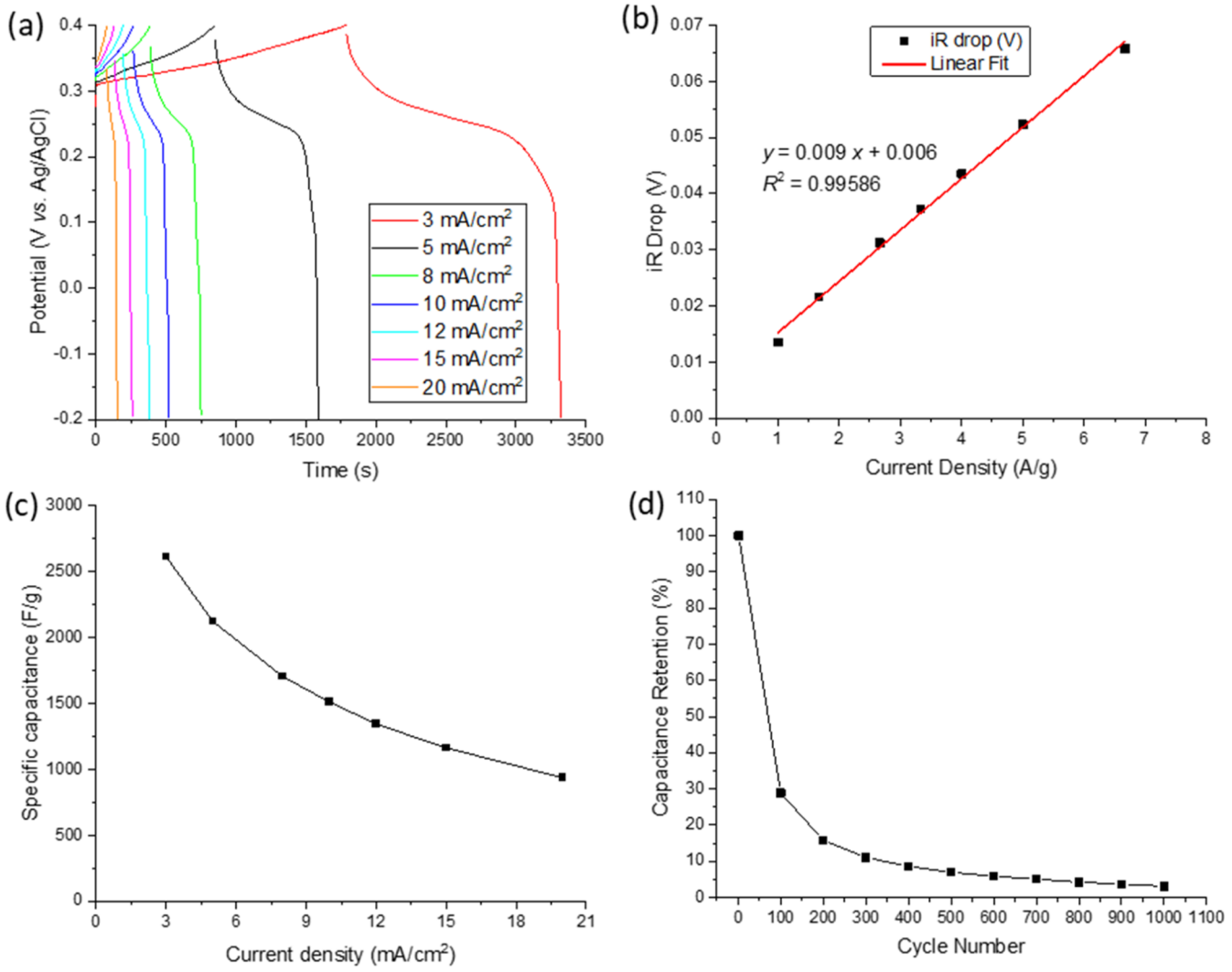

Figure 5. (a) GCD plots under the potential window of −0.2 to 0.4 V at different current densities. (b) Linear fit of current densities vs iR drops. (c) From GCD curves (a) using eq 1 to calculate specific capacitance (F/g) at various current densities. (d) Cycling performance of the 3D NC-rGO@Ni-foam electrode over 1000 GCD cycles.

symmetrical triangular curve for EDLCs and a flat line for PCs. This method is often used to assess capacitance, rate capabilities, and cycling stability.[47−49] EIS is commonly utilized to analyze charge storage mechanisms, charge transfer, and mass transport. This dielectric spectroscopic technique measures the impedance of a test cell across different frequencies by applying a low-amplitude AC voltage, typically set at 5 mV. EIS consists of two main plots: the Nyquist plot, which displays the imaginary and real components of the cell's impedances, and the Bode plot, which illustrates the relationship between phase angle and frequency. Equivalent circuits help identify each structural component's contribution to the cell models' overall impedance.[9,47,50,51]

The C_s (F/g) of the materials in both the 3-electrode (eq 1) and Swagelok cell (eq 2) designs were estimated from the resulting equations.[9,52]

$$C_s = \left(\frac{I \times \Delta t}{m \times \Delta V}\right) \quad (1)$$

$$C_s = \left(\frac{4 \times I \times \Delta t}{M \times \Delta V}\right) \quad (2)$$

where I is the discharge current, t is the discharge time, m is the mass of the active material, V is the discharge voltage window, and M is the total mass of two electrodes. Parameters such as E and P are crucial in assessing the electrochemical performance of energy storage devices, forming the foundation for practical applications.[9] The E signifies the quantity of electrical energy stored and deliverable, which can be calculated gravimetrically using eq 3. On the other hand, the P characterizes the efficiency in energy uptake/delivery, and it can be obtained utilizing eq 4.[53]

$$E = (1/2) \times C_s \times V^2 \times (1/3.6) \quad (3)$$

$$P = E/t \quad (4)$$

where C_s is the specific capacitance, V represents the voltage between two electrodes, Q denotes the total accumulated charges, and t is the discharge time.

3.3.1. Electrochemical Examination Results for 3-Electrode Cell. After the potential window has been determined between −0.4 and 0.9 V, Figure 4a compares the cleaned bare Ni-foam CV curve and the 3D NC-rGO@Ni-foam electrode CV curve at a scan rate of 20 mV/s. The area under the CV

https://doi.org/10.1021/acsomega.4c10988
ACS Omega 2025, 10, 16457−16471

Table 2. Comparison of Electrochemical Properties of Previously Published Research with the 3D NC-rGO@Ni-Foam Electrode Material

materials	potential range (V)	current density (A/g)	specific capacitance (F/g)	electrolyte	refs
3D NC-rGO@Ni-foam	0.6	1	2612	2 M KOH	this work
3D NF/G/Ni−Co−S	0.8	2	2526	6 M KOH	42
$NiCo_2O_4$/rGO/NF	0.7	1	2682.6	6 M KOH	32
NCO-rGO	0.6	0.73	265	1 M Na_2SO_4	13
NRGO−$NiCoO_2$	0.5	0.5	508	3 M KOH	61
$NiCo_2O_4$/rGO	0.6	1	1380	6 M KOH	62
NiCoLDH@rGO	0.5	1.5	963 C/g	1 M KOH	63
$NiCo_2O_4$/GO	0.5	1	1211.2	6 M KOH	64

curves represents the charge stored by the electrode materials, and the area of the CV curve of 3D NC-rGO@Ni-foam is way bigger than that of the area of the CV curve of the bare Ni-foam. In addition, the notable redox behavior displayed by the 3D NC-rGO@Ni-foam shows a significant redox capacitance contribution from the synthesized material, surpassing that of bare Ni-foam. In Figure 4b, all the CV curves reveal a pair of redox peaks at different scan rates ranging from 2 to 100 mV/s. This indicates that Faradaic redox reactions primarily dominate the charge transport properties, unlike the usual CV curves produced by EDLCs. The anodic peak at 0.4 V is linked to the oxidation process, while the cathodic peak at 0.2 V is associated with the reverse oxidation process, as seen at a low scan rate of 2 mV/s in Figure 4b. The anodic peak at 0.4 V may be attributed to the following electrochemical equation.[54,55]

$$Ni + 2OH^- \leftrightarrow Ni(OH)_2 + 2e^- \quad (5)$$

At higher potential, redox couple Ni(II)/Ni(III) is formed according to the equation below[54,55]

$$Ni(OH)_2 + OH^- \leftrightarrow NiOOH + H_2O + e^- \quad (6)$$

With the scan rate rising from 2 to 100 mV/s, distinct shifts in the redox peak positions were observed in the CV profiles. Figure 4c illustrates a linear relationship between the oxidative and reductive current density values and the square root of the scan rates, suggesting that the electrochemical energy storage reaction of the 3D NC-rGO@Ni-foam electrode follows a diffusion-controlled process.[56,57] To further investigate the charge storage kinetics, Dunn's method was applied to differentiate and quantify capacitive and diffusive charge storage contributions. At low scan rates (≤20 mV/s), the CV profiles exhibit distinct redox peaks, indicating the coexistence of the Faradaic (diffusion current controlled) and non-Faradaic process (capacitive current controlled due to double layer formation) charge storage mechanisms. Figure 4d illustrates the capacitive and diffusive current contributions in a bar diagram. At 2 mV/s, the diffusion-controlled process dominates, accounting for 80.04% of the total charge storage, while the capacitive contribution is 19.96%. As the scan rate increases to 20 mV/s, the diffusion-controlled contribution decreases to 55.90%, with the capacitive contribution rising to 44.10%, indicating a greater reliance on surface-driven charge storage at higher scan rates. The 3D NC-rGO@Ni-foam electrode operates mainly through a diffusion-controlled charge storage mechanism. As the scan rate rises, the capacitive contributions gain importance. This phenomenon is linked to the electrode's highly porous 3D structure that promotes ion transport, reduces diffusion distances, and boosts redox reactions, improving energy storage efficiency.

The GCD profiles of the 3D NC-rGO@Ni-foam electrode at various current densities ranging from 3 to 20 mA/cm^2 in the potential range of −0.2 to 0.4 V are depicted in Figure 5a. The oxidative peak voltage in the CV curve determined the potential range selected for the GCD measurement. This peak potential was deliberately selected to avoid saturation of the charging time at low current densities, enabling the charging process to achieve its limit at these lower densities. Figure 5b displays a linear fit of the iR drop against current density. The initial iR drop noted at the start of every GCD profile signifies resistance to normal internal conditions.[58] The internal resistance is a combination of resistances of the electrode, the electrolyte, the separator, the current collector, and the contact.[58,59] At higher current values, the ions exhibit greater resistance to the electrodes compared to lower charge−discharge rates. All the iR drops are quite small values (<0.07 V), illustrating low resistance for the diffusion of electrolyte ions within the electrode in KOH aqueous electrolyte.

The specific capacitance values were derived from the GCD curves using eq 1. These values are shown in Figure 5c. The measured specific capacitance values were 2612, 2124, 1705, 1512, 1345, 1164, and 937 F/g at current densities of 3, 5, 8, 10, 12, 15, and 20 mA/cm^2, respectively. The gravimetric performance was assessed based on the mass loading of the 3D NC-rGO@Ni-foam electrode (3 mg/cm^2). This electrode demonstrated exceptional capacitance, and to highlight the benefits of this nanonetwork, the specific capacitance values were compared with those reported in the existing literature, as detailed in Table 2. Compared to the publications listed, our 3D NC-rGO@Ni-foam demonstrates the capability to operate within a wide potential window while exhibiting relatively higher Cs and requiring lower electrolyte concentrations. The nearly highest specific capacitance is attributed to several structural features of the binder-free 3D NC-rGO@Ni-foam electrode. Initially, employing Ni-foam as a substrate creates numerous pores, thereby enlarging the active surface area. Subsequently, the reduction of GO to rGO enhances the electrical conductivity of the electrode. Additionally, the combination of nickel and cobalt metals boosts the capacitance. Furthermore, the nanoflower morphology of the 3D NC-rGO contributes to the electrode having the largest active surface area, ensuring a favorable capacitance. Lastly, the binder-free electrode minimizes the reduction in electrical conductivity that typically arises from using binder materials.

The investigation into the long-cycle stability of the electrode material spanned 1000 GCD cycles. As illustrated in Figure 5d, the capacitance retention declined to 29.5% from the first cycle to the 100th cycle. It is noteworthy that the capacitance demonstrated a tendency to stabilize after 200 cycles of GCD tests, with fluctuations in capacitance retention

https://doi.org/10.1021/acsomega.4c10988
ACS Omega 2025, 10, 16457−16471

within 15%, particularly evident at a current density of 5 A/g. However, it is observed that the cycling stability of the 3D NC-rGO@Ni-foam is suboptimal. Two primary reasons contribute to this: First, as a binder-free electrode material, the fabrication process omitted the use of binder materials, which typically enhance the adhesion of the active material with the substrate. Second, the low current density of 5 A/g used in the cycling stability tests may have influenced the results. It is recognized that materials tend to display improved cyclic stability at higher current densities or scan rates under similar conditions rates.[60] For instance, in Lv's study, they synthesized $NiCo_2O_4$/rGO on Ni-foam, achieving a cycling stability of 75% at 50 A/g.[32]

EIS tests indicate both electrode materials' resistance and electrolyte ions' diffusion. Figure 6 shows the Nyquist plot for the 3D NC-rGO@Ni-foam electrode before and after 1000 GCD cycles. In the high-frequency area, the beginning of the semicircle indicates the equivalent series resistance (R_s), which reflects the electrical conductivity of the electrodes. This includes the electrolyte's ionic resistance, the materials' intrinsic resistance, and the contact resistance at the interface between the electroactive material and the surface-active substance (current collector).[65] It can be observed that the 3D NC-rGO@Ni-foam electrode exhibits small R_s of approximately 1.0 Ω (before GCD) and 1.1 Ω (after GCD), indicating improved electrical conductivity of the electrodes, in the high-frequency regions, the semicircle indicates the charge transfer resistances (R_p) and the movement of ions at the electrode/electrolyte interface.[66] The R_p observed before (3.3 Ω) and after (8.9 Ω) the cycling demonstrates the excellent electrochemical behavior of the electrode. At the same time, the absence of a distinct semicircle for the 3D NC-rGO@Ni-foam before GCD indicates a rapid charge transfer rate, signifying good contact between the active material and the current collector. In the low-frequency region, the Nyquist plots exhibit a nearly 45° straight line relative to the real axis, suggesting the presence of the electrolyte's diffusive resistance (Warburg resistance) within the electrode pores,[67,68] which corresponds well with the CV results regarding the relationship between current density and the square root of scan rates. The transition between the high-frequency (semicircle) and low-frequency components (straight line) is often referred to as the "knee". This "knee" slope reflects the power capability of the supercapacitor.[53,69,70] A higher slope observed in the before GCD curve suggests that the 3D NC-rGO@Ni-foam electrode initially exhibits smaller electrolyte ion diffusion resistance and shorter diffusion distance. From the above analysis, we can see that the 3D NC-rGO@Ni-foam has the advantage of good capacitor characteristics as the electrode materials of the supercapacitors.

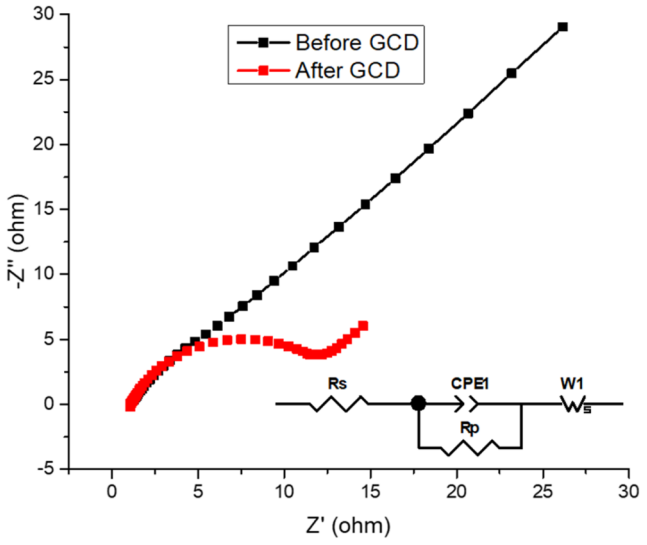

Figure 6. Nyquist plot before and after 1000 cycles of GCD and the equivalent circuit.

3.3.2. Electrochemical Examination Results for Swagelok Cell. To explore the full capacitor behavior, we constructed a symmetric capacitor utilizing the 3D NC-rGO@Ni-foam as both the negative and positive electrodes of the Swagelok cell. The voltage of the assembled Swagelok cell was extended to 2.5 V. Under this potential range, Figure 7(a) illustrates the CV curves of symmetric supercapacitor devices at various scan rates ranging from 2 to 100 mV/s. The shapes of the CV profiles appear squarer compared to Figure 4b, indicating improved behavior characteristics of EDLCs. The 24 h self-

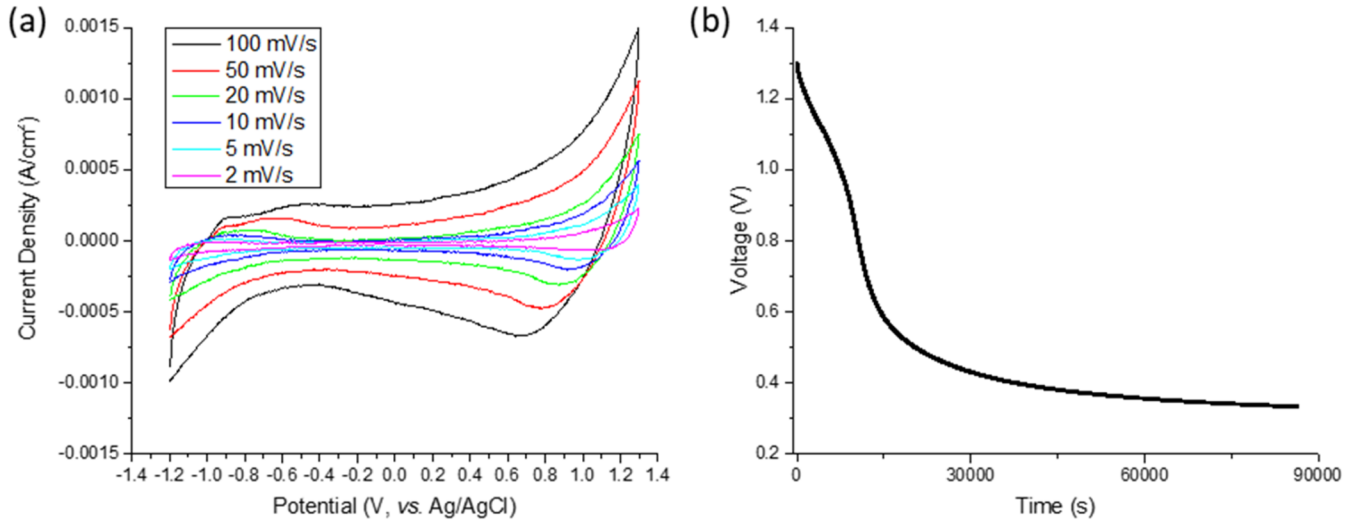

Figure 7. (a) CV curves for the Swagelok cell at various scan rates under a potential range between −1.2 to 1.3 V. (b) Self-discharge curve of the symmetric 3D NC-rGO@Ni-foam.

https://doi.org/10.1021/acsomega.4c10988
ACS Omega 2025, 10, 16457−16471

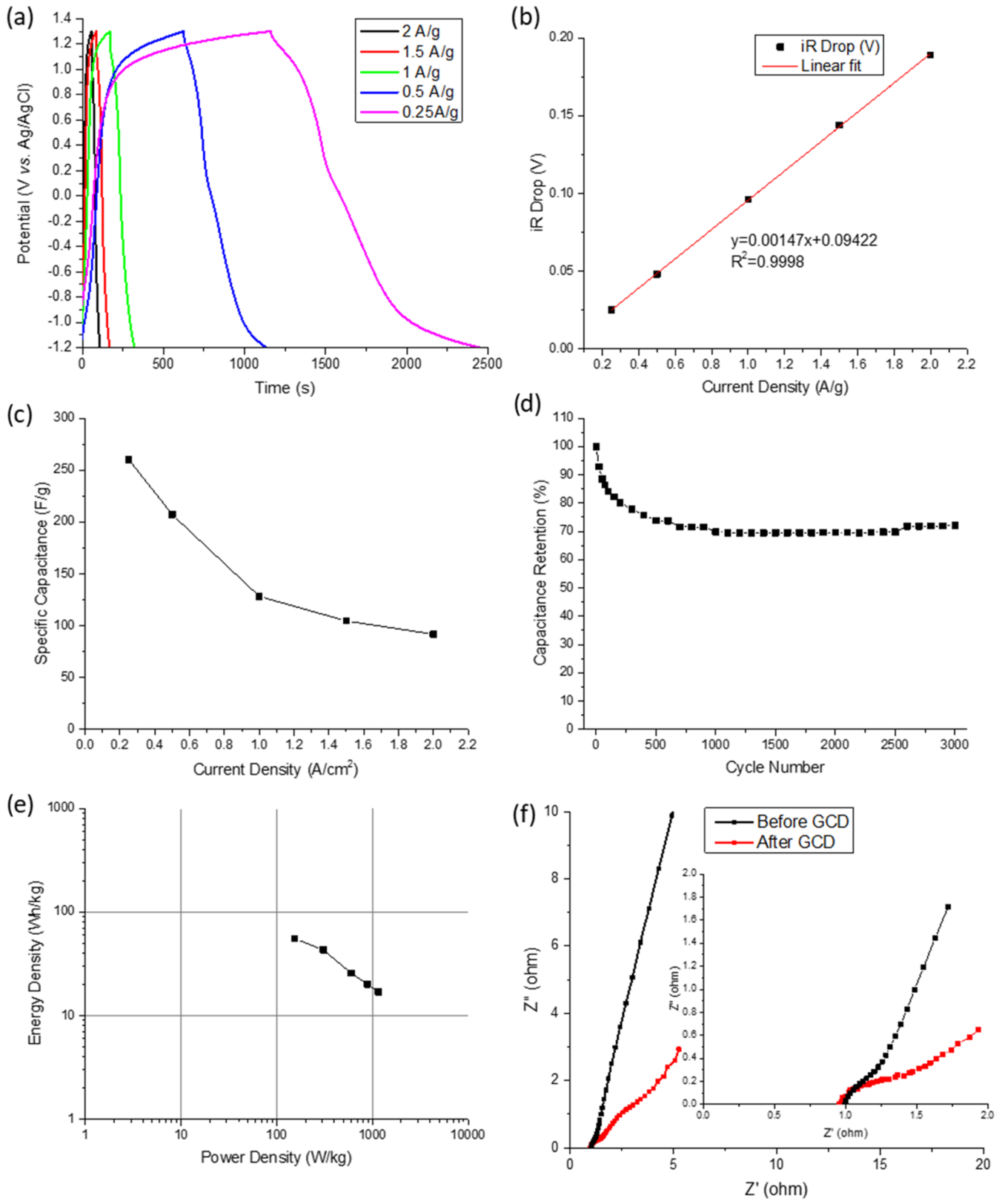

Figure 8. Electrochemical performances of a Swagelok system of symmetric 3D NC-rGO@Ni-foam. (a) GCD plots at different current densities. (b) The linear fit of iR drops at different current densities. (c) Calculated specific capacitance (F/g) at various current densities. (d) Cycling performance over 3000 GCD cycles. (e) Ragone plot. (f) Nyquist plots.

discharge profile of a two-electrode Swagelok cell, following a 2 h potentiostatic hold at 1.3 V, is presented in Figure 7b. The voltage exhibits a rapid initial decline within the first few hours after the circuit is opened, which is primarily attributed to the redistribution of charge within the electrode material and the discharge of surface-adsorbed species. As time progresses, the

https://doi.org/10.1021/acsomega.4c10988
ACS Omega 2025, 10, 16457−16471

Table 3. Comparison of Electrochemical Properties of Previously Published Research with Our Symmetric Supercapacitor Device

materials	capacitor type	C_s (F/g)	energy density (Wh/kg)	power density (W/kg)	potential range (V)	capacitance retention (cycles)	refs
3D NC-rGO@Ni-foam	symmetric	260	55	155	2.5	72% (3000th, 2 A/g)	this work
NCO-rGO	ASSCs	131	47	631	1.6	69% (1000th, 1 A/g)	13
$NiCo_2O_4$/rGO/NF	symmetric	291.5	35	12,000	1.2	180% (14,000th, 10 A/g)	32
NRGO−$NiCoO_2$	flexible SPs	58			0.8	94% (2000th, 1 A/g)	61
NiCoLDH//rGO	ASSCs		56	810	1.8	99%, (10,000th, 5 A/g)	63
$NiCo_2O_4$/GO	ASSCs	144.45	51.36	50,000	1.6	88.6% (2000th, 8 A/g)	64

rate of voltage drop decreases, indicating a transition from surface-related charge loss to slower, diffusion-limited processes. This behavior suggests that while some self-discharge is inevitable due to charge relaxation and internal resistance effects, the electrode material retains a significant fraction of its stored energy over extended periods, demonstrating its potential for practical energy storage applications.

Figure 8a displays the GCD profiles of the symmetric supercapacitor at various current densities ranging from 0.25 to 2 A/g within the potential window from −1.2 to 1.3 V. The GCD profile shapes appear more triangular than those in Figure 5a, indicating improved behavior characteristics of EDLCs. Figure 8b shows a linear fit of the iR drop profiles collected at different current densities. Similar to 3-electrode cells operating at higher current densities, ions demonstrate increased resistance to the electrodes compared to lower charge−discharge rates. The iR drops are minimal, indicating low resistance for the diffusion of electrolyte ions through the electrodes in KOH aqueous electrolyte. The specific capacitance values were calculated using the discharge time from these GCD profiles, as illustrated in Figure 8c. The estimated specific capacitance values at various current densities ranged from 260.2 to 91.8 F/g at 0.25 to 2 A/g. Figure 8d illustrates the capacitance retention for the symmetric supercapacitor over 3000 GCD cycles, reaching 72% from the initial to 3000th cycles at a current density of 2 A/g. From cycle 200th (80% retention) to 3000th, the retention change is less than 10%, which indicates the device reached performance stability after 200 cycles of GCD. The cycling stability of the symmetric supercapacitor device significantly surpasses that of the previous 3-electrode system. Compared with previously published works (Table 3), our work's current density is comparable or even 4 to 5 times smaller than that some previous works. Still, the potential window is way broader than the others. Additionally, Figure 8e presents the Ragone plot of the symmetric supercapacitor device, revealing a high energy density of 55 Wh/kg and a power density of 155 W/kg. The symmetric supercapacitor device employing the 3D NC-rGO@Ni-foam exhibited a relatively higher energy density than previous literature, as summarized in Table 3.

Additionally, Figure 8f shows the Nyquist plot for the symmetric supercapacitor device, captured at frequencies between 10 mHz and 100 kHz. The equivalent series resistances (R_s) of approximately 1.02 Ω (before GCD) and 0.86 Ω (after GCD), along with charge transfer resistance (R_p) values of 0.26 Ω (before GCD) and 5.4 Ω (after GCD), underscore the excellent electrochemical properties of the assembled symmetric supercapacitor device. Compared with prior research, ASSCs typically exhibit higher C_s and E than symmetric supercapacitors. However, our symmetric supercapacitor device boasts a broader potential window, relatively higher C_s and E and lower P than the listed studies.

4. CONCLUSIONS

In summary, the binder-free 3D NC-rGO@Ni-foam was successfully synthesized via a one-step hydrothermal method supported by a wet-chemical approach. The in situ development of the 3D NC-rGO nanonetwork on Ni-foam is expected to improve charge-storage capacitance. Meanwhile, the porous structure of the 3D NC-rGO@Ni-foam aids in the penetration and diffusion of electrolyte ions during redox reactions, leveraging the electronic conductivity of rGO. The electrochemical performance of the 3D NC-rGO@Ni-foam electrode materials exhibited an exceptional specific capacitance of 2612 F/g at a current density of 1 A/g. The structural advantages of the 3D NC-rGO@Ni-foam nanonetwork enable ultrahigh capacitance and long-term cycling performance. Moreover, the fabricated symmetric supercapacitor device exhibited a relatively high energy density of 55 Wh/kg at a power density of 155 W/kg and 72% capacity retention over 3000 cycles of GCD at a current density of 2 A/g, indicating excellent durability. The remarkable retention and 2.5 V capability suggest promising practical applications in electronic devices. With its straightforward synthesis, feasible electrochemical performance, and high energy density, the binder-free 3D NC-rGO@Ni-foam nanonetworks hold potential as redox-type electrodes for high-performance energy storage devices.

AUTHOR INFORMATION

Corresponding Author

Julia Xiaojun Zhao − *Department of Chemistry, University of North Dakota, Grand Forks, North Dakota 58202-8358, United States;* orcid.org/0000-0002-9603-666X; Phone: 701-777-3610; Email: Julia.zhao@und.edu; Fax: 701-777-2331

Authors

Wen Sun − *Department of Chemistry, University of North Dakota, Grand Forks, North Dakota 58202-8358, United States;* orcid.org/0000-0002-4172-5177

Mehmet Ozdogan − *Department of Physics & Astrophysics, University of North Dakota, Grand Forks, North Dakota 58202-8358, United States*

Nuri Oncel − *Department of Physics & Astrophysics, University of North Dakota, Grand Forks, North Dakota 58202-8358, United States;* orcid.org/0000-0002-0292-3349

Complete contact information is available at: https://pubs.acs.org/10.1021/acsomega.4c10988

https://doi.org/10.1021/acsomega.4c10988
ACS Omega 2025, 10, 16457−16471

Author Contributions

W.S.: Conceptualization, Methodology, Data curation, Writing—original draft, Visualization, Investigation, Validation, taken the photo in Scheme [1]. M.O.: XPS analysis. N.O.: XPS analysis. J.X.Z.: Conceptualization, Methodology, Supervision.

Funding

This work is partially supported by the National Science Foundation grant CHE 2304873. The Metal Analysis Core Facility at North Dakota INBRE receives support from NIH grant 5P20GM103442−18 and the University of North Dakota's Department of Chemistry.

Notes

The authors declare no competing financial interest.

■ ACKNOWLEDGMENTS

The ICP-MS analysis at the North Dakota INBRE Metal Analysis Core Facility was partially funded by NIH grant 5P20GM103442-18. We extend our gratitude to Prof. David T. Pierce from the University of North Dakota for his invaluable experimental assistance. His expertise, guidance, and contributions to the experimental aspects of this work were instrumental in advancing the research. We deeply appreciate his generosity in sharing his time, knowledge, and resources.

■ ABBREVIATIONS

NC-rGO@Ni-foam, nickel cobalt with reduced graphene oxide at nickel foam; SCs, supercapacitors; EDLCs, electrical double-layer capacitors; PCs, pseudocapacitors; GO, graphene oxide; rGO, reduced graphene oxide; C_s, specific capacitance; E, energy density; P, power density; GF, graphene foam; ASSCs, asymmetric supercapacitors; TMOs, transition metal oxides; NCO-QDs, nickel cobalt oxide quantum dots; NCO-rGO, nickel cobalt oxide on reduced graphene oxide; M^{2+}, divalent transition metal ions; Ni-foam, nickel foam; 3D, three-dimensional; DI water, deionized water; SEM, scanning electron microscopy; EDS, energy dispersive spectroscopy; XRD, X-ray diffraction; XPS, X-ray photoelectron spectroscopy; ICP-MS, inductively coupled plasma mass spectrometry; CV, cyclic voltammetry; GCD, galvanostatic charge−discharge; EIS, electrochemical impedance spectroscopy; WE, working electrode; CE, counter electrode; RE, reference electrode; OCP, open circuit potential

■ REFERENCES

(1) Miller, J. R.; Simon, P. Electrochemical capacitors for energy management. *Science* **2008**, *321* (5889), 651−652.
(2) Pandolfo, A. G.; Hollenkamp, A. F. Carbon properties and their role in supercapacitors. *J. Power Sources* **2006**, *157* (1), 11−27.
(3) Chu, S.; Majumdar, A. Opportunities and challenges for a sustainable energy future. *Nature* **2012**, *488* (7411), 294−303.
(4) Shao, Y.; El-Kady, M. F.; Sun, J.; Li, Y.; Zhang, Q.; Zhu, M.; Wang, H.; Dunn, B.; Kaner, R. B. Design and mechanisms of asymmetric supercapacitors. *Chem. Rev.* **2018**, *118* (18), 9233−9280.
(5) Simon, P.; Gogotsi, Y.; Dunn, B. Where do batteries end and supercapacitors begin? *Science* **2014**, *343* (6176), 1210−1211.
(6) Winter, M.; Brodd, R. J. What are batteries, fuel cells, and supercapacitors? *Chem. Rev.* **2004**, *104* (10), 4245−4270.
(7) Simon, P.; Gogotsi, Y. Materials for Electrochemical Capacitors. In *Nanoscience and Technology*; Co-Published with Macmillan Publishers Ltd.: UK, 2009; pp 320−329.
(8) Liu, Y.; Deng, R.; Wang, Z.; Liu, H. Carboxyl-functionalized graphene oxide-polyaniline composite as a promising supercapacitor material. *J. Mater. Chem.* **2012**, *22* (27), 13619−13624.
(9) Chang, L.; Hang Hu, Y.2.21 Supercapacitors. In *Comprehensive Energy Systems*; Elsevier, 2018; pp 663−695.
(10) Panda, P. K.; Grigoriev, A.; Mishra, Y. K.; Ahuja, R. Progress in supercapacitors: roles of two dimensional nanotubular materials. *Nanoscale Adv.* **2020**, *2* (1), 70−108.
(11) Chang, L.; Hu, Y. H. Breakthroughs in designing commercial-level mass-loading graphene electrodes for electrochemical double-layer capacitors. *Matter* **2019**, *1* (3), 596−620.
(12) Wang, G.; Zhang, L.; Zhang, J. A review of electrode materials for electrochemical supercapacitors. *Chem. Soc. Rev.* **2012**, *41* (2), 797−828.
(13) Siwatch, P.; Sharma, K.; Singh, N.; Manyani, N.; Tripathi, S. K. Enhanced supercapacitive performance of reduced graphene oxide by incorporating $NiCo_2O_4$ quantum dots using aqueous electrolyte. *Electrochim. Acta* **2021**, *381*, No. 138235.
(14) Nallapureddy, J.; Pallavolu, M. R.; Babu, P. S. S.; Al-Asbahi, B. A.; Joo, S. W. Designed construction of hierarchical cobalt sulfide nanonetwork as a high-capacity and binder-free cathode for hybrid supercapacitors. *Energy Fuels* **2023**, *37* (22), 17535−17544.
(15) Majumdar, D.; Baugh, N.; Bhattacharya, S. K. Ultrasound assisted formation of reduced graphene oxide-copper (II) oxide nanocomposite for energy storage applications. *Colloids Surf., A* **2017**, *512*, 158−170.
(16) Yu, M.; Wang, Z.; Han, Y.; Tong, Y.; Lu, X.; Yang, S. Recent progress in the development of anodes for asymmetric supercapacitors. *J. Mater. Chem. A* **2016**, *4* (13), 4634−4658.
(17) Novoselov, K. S.; Fal'ko, V. I.; Colombo, L.; Gellert, P. R.; Schwab, M. G.; Kim, K. A roadmap for graphene. *Nature* **2012**, *490* (7419), 192−200.
(18) Gao, W.; Alemany, L. B.; Ci, L.; Ajayan, P. M. New insights into the structure and reduction of graphite oxide. *Nat. Chem.* **2009**, *1* (5), 403−408.
(19) Hu, H.; Zhao, Z.; Zhang, R.; Bin, Y.; Qiu, J. Polymer casting of ultralight graphene aerogels for the production of conductive nanocomposites with low filling content. *J. Mater. Chem. A* **2014**, *2* (11), 3756−3760.
(20) Shen, J.; Li, T.; Huang, W.; Long, Y.; Li, N.; Ye, M. One-pot polyelectrolyte assisted hydrothermal synthesis of RuO_2-reduced graphene oxide nanocomposite. *Electrochim. Acta* **2013**, *95*, 155−161.
(21) Yan, J.; Wei, T.; Shao, B.; Ma, F.; Fan, Z.; Zhang, M.; Zheng, C.; Shang, Y.; Qian, W.; Wei, F. Electrochemical properties of graphene nanosheet/carbon black composites as electrodes for supercapacitors. *Carbon* **2010**, *48* (6), 1731−1737.
(22) Kang, D.; Liu, Q.; Gu, J.; Su, Y.; Zhang, W.; Zhang, D. "Egg-box"-assisted Fabrication of porous carbon with small mesopores for high-rate electric double layer capacitors. *ACS Nano* **2015**, *9* (11), 11225−11233.
(23) Sun, W.; Sahin, N. E.; Sun, D.; Wu, X.; Munoz, C.; Thakare, J.; Aulich, T.; Zhang, J.; Hou, X.; Oncel, N.; Pierce, D.; Zhao, J. X. One-pot synthesis of ruthenium-based nanocatalyst using reduced graphene oxide as matrix for electrochemical synthesis of ammonia. *ACS Appl. Mater. Interfaces* **2023**, *15* (1), 1115−1128.
(24) Wu, X.; Xing, Y.; Pierce, D.; Zhao, J. X. One-pot synthesis of reduced graphene oxide/metal (oxide) composites. *ACS Appl. Mater. Interfaces* **2017**, *9* (43), 37962−37971.
(25) Liu, Y.; Wang, Z.; Veder, J.-P. M.; Xu, Z.; Zhong, Y.; Zhou, W.; Tade, M. O.; Wang, S.; Shao, Z. Highly defective layered double perovskite oxide for efficient energy storage via reversible pseudocapacitive oxygen-anion intercalation. *Adv. Energy Mater.* **2018**, *8* (11), No. 1702604.
(26) Zhi, M.; Xiang, C.; Li, J.; Li, M.; Wu, N. Nanostructured carbon-metal oxide composite electrodes for supercapacitors: a review. *Nanoscale* **2013**, *5* (1), 72−88.
(27) Dubal, D. P.; Gomez-Romero, P.; Sankapal, B. R.; Holze, R. Nickel cobaltite as an emerging material for supercapacitors: An overview. *Nano Energy* **2015**, *11*, 377−399.
(28) Poonam; Sharma, K.; Singh, N.; Tripathi, S. K. Characterization of nickel cobalt oxide: a potential material for supercapacitor. *Mater. Res. Express* **2019**, *6* (2), No. 025502.

https://doi.org/10.1021/acsomega.4c10988
ACS Omega 2025, 10, 16457−16471

(29) Nath, N. C. D.; Lee, J.-J. Intercalation-type electrodes of copper-cobalt oxides for high-energy-density supercapacitors. *J. Electroanal. Chem.* **2020**, *861*, No. 113947.
(30) Hassan, H. K.; Atta, N. F.; Hamed, M. M.; Galal, A.; Jacob, T. Ruthenium nanoparticles-modified reduced graphene prepared by a green method for high-performance supercapacitor application in neutral electrolyte. *RSC Adv.* **2017**, *7* (19), 11286−11296.
(31) Yang, D.; Zhao, Q.; Huang, L.; Xu, B.; Kumar, N. A.; Zhao, X. S. Encapsulation of $NiCo_2O_4$ in nitrogen-doped reduced graphene oxide for sodium ion capacitors. *J. Mater. Chem. A* **2018**, *6* (29), 14146−14154.
(32) Lv, A.; Lu, S.; Xu, W.; Wang, Z.; Shen, Y.; Liu, G. One-pot synthesis of $NiCo_2O_4$/rGO/NF hybrid electrode materials realizing ultrahigh capacitance and rapid charge/discharge at large current density. *Appl. Surf. Sci.* **2020**, *511*, No. 145538.
(33) Kaur, M.; Chand, P.; Anand, H.; Aarti. Fabrication of asymmetric supercapacitor device with $NiCo_2O_4$@reduced graphene oxide nanocomposites. *Electrochim. Acta* **2024**, *507*, No. 145118.
(34) Kim, T. H.; Veerasubramani, G. K.; Kim, S. J. Hierarchical porous flower-like nickel cobaltite nanosheets as a binder-less electrode for supercapacitor application with ultra-high capacitance. *J. Ind. Eng. Chem.* **2018**, *61*, 181−187.
(35) Wang, S.; Sun, S.; Li, S.; Gong, F.; Li, Y.; Wu, Q.; Song, P.; Fang, S.; Wang, P. Time and temperature dependent multiple hierarchical $NiCo_2O_4$ for high-performance supercapacitors. *Dalton Trans.* **2016**, *45* (17), 7469−7475.
(36) Qiu, Y.; Li, X.; Bai, M.; Wang, H.; Xue, D.; Wang, W.; Cheng, J. Pseudocapacitive behaviors of mesoporous nickel-cobalt oxide nanoplate electrodes in different electrolyte systems. *New J. Chem.* **2017**, *41* (5), 2124−2130.
(37) Yu, J.; Wang, Q.; O'Hare, D.; Sun, L. Preparation of two dimensional layered double hydroxide nanosheets and their applications. *Chem. Soc. Rev.* **2017**, *46* (19), 5950−5974.
(38) Cai, X.; Shen, X.; Ma, L.; Ji, Z.; Xu, C.; Yuan, A. Solvothermal synthesis of NiCo-layered double hydroxide nanosheets decorated on RGO sheets for high performance supercapacitor. *Chem. Eng. J.* **2015**, *268*, 251−259.
(39) Chen, H.; Hu, L.; Chen, M.; Yan, Y.; Wu, L. Nickel-cobalt layered double hydroxide nanosheets for high-performance supercapacitor electrode materials. *Adv. Funct. Mater.* **2014**, *24* (7), 934−942.
(40) Lu, Y.; Yan, H.; Zhang, D.; Lin, J.; Xue, Y.; Li, J.; Luo, Y.; Tang, C. Hybrid nanonet/nanoflake $NiCo_2O_4$ electrodes with an ultrahigh surface area for supercapacitors. *J. Solid State Electrochem.* **2014**, *18* (11), 3143−3152.
(41) Jiang, X.; Ma, Y.; Li, J.; Fan, Q.; Huang, W. Self-assembly of reduced graphene oxide into three-dimensional architecture by divalent ion linkage. *J. Phys. Chem. C* **2010**, *114* (51), 22462−22465.
(42) Miao, P.; He, J.; Sang, Z.; Zhang, F.; Guo, J.; Su, D.; Yan, X.; Li, X.; Ji, H. Hydrothermal growth of 3D graphene on nickel foam as a substrate of nickel-cobalt-sulfur for high-performance supercapacitors. *J. Alloys Compd.* **2018**, *732*, 613−623.
(43) Grote, F.; Yu, Z.-Y.; Wang, J.-L.; Yu, S.-H.; Lei, Y. Self-stacked reduced graphene oxide nanosheets coated with cobalt-nickel hydroxide by one-step electrochemical deposition toward flexible electrochromic supercapacitors. *Small* **2015**, *11* (36), 4666−4672.
(44) Mendes, A. S. S. Analysis of Micro and Nanoplastics with X-ray Photoelectron Spectroscopy. 2022.
(45) Zaanen, J.; Sawatzky, G. A. Strong interference between decay channels and valence-electron rearrangements in core-hole spectroscopy. *Phys. Rev. B* **1986**, *33* (12), No. 8074.
(46) Elgrishi, N.; Rountree, K. J.; McCarthy, B. D.; Rountree, E. S.; Eisenhart, T. T.; Dempsey, J. L. A Practical beginner's guide to cyclic voltammetry. *J. Chem. Educ.* **2018**, *95* (2), 197−206.
(47) Stoller, M. D.; Ruoff, R. S. Best practice methods for determining an electrode material's performance for ultracapacitors. *Energy Environ. Sci.* **2010**, *3* (9), 1294−1301.
(48) Rauhala, T.; Leis, J.; Kallio, T.; Vuorilehto, K. Lithium-ion capacitors using carbide-derived carbon as the positive electrode—A comparison of cells with graphite and $Li_4Ti_5O_{12}$ as the negative electrode. *J. Power Sources* **2016**, *331*, 156−166.
(49) Zhang, X.; Romm, M.; Zheng, X.; Zink, E. M.; Kim, Y.-M.; Burnum-Johnson, K. E.; Orton, D. J.; Apffel, A.; Ibrahim, Y. M.; Monroe, M. E.; Moore, R. J.; Smith, J. N.; Ma, J.; Renslow, R. S.; Thomas, D. G.; Blackwell, A. E.; Swinford, G.; Sausen, J.; Kurulugama, R. T.; Eno, N.; Darland, E.; Stafford, G.; Fjeldsted, J.; Metz, T. O.; Teeguarden, J. G.; Smith, R. D.; Baker, E. S. SPE-IMS-MS: An automated platform for sub-sixty second surveillance of endogenous metabolites and xenobiotics in biofluids. *Clin. Mass Spectrom.* **2016**, *2*, 1−10.
(50) Tripathy, M. C.; Mondal, D.; Biswas, K.; Sen, S. Experimental studies on realization of fractional inductors and fractional-order bandpass filters. *Int. J. Circuit Theory Appl.* **2015**, *43* (9), 1183−1196.
(51) Lazanas, A. C.; Prodromidis, M. I. Electrochemical impedance spectroscopy-A tutorial. *ACS Meas. Sci. Au* **2023**, *3* (3), 162−193.
(52) Zhu, J.; Zhang, Q.; Guo, L.; Zhao, Y.; Zhang, R.; Liu, L.; Yu, J. Highly flexible, freestanding supercapacitor electrodes based on hollow hierarchical porous carbon nanofibers bridged by carbon nanotubes. *Chem. Eng. J.* **2022**, *434*, No. 134662.
(53) Deb Nath, N. C.; Jeon, I.-Y.; Ju, M. J.; Ansari, S. A.; Baek, J.-B.; Lee, J.-J. Edge-carboxylated graphene nanoplatelets as efficient electrode materials for electrochemical supercapacitors. *Carbon* **2019**, *142*, 89−98.
(54) Ashok, A.; Kumar, A.; Ponraj, J.; Mansour, S. A.; Tarlochan, F. Single step synthesis of porous $NiCoO_2$ for effective electrooxidation of glycerol in alkaline medium. *J. Electrochem. Soc.* **2018**, *165* (15), No. J3301.
(55) Oliveira, V. L.; Morais, C.; Servat, K.; Napporn, T. W.; Tremiliosi-Filho, G.; Kokoh, K. B. Glycerol oxidation on nickel based nanocatalysts in alkaline medium-Identification of the reaction products. *J. Electroanal. Chem.* **2013**, *703*, 56−62.
(56) Wu, M.-S.; Lyu, L.-J.; Syu, J.-H. Copper and nickel hexacyanoferrate nanostructures with graphene-coated stainless steel sheets for electrochemical supercapacitors. *J. Power Sources* **2015**, *297*, 75−82.
(57) Krishnan, S. G.; Rahim, M. H. A.; Jose, R. Synthesis and characterization of $MnCo_2O_4$ cuboidal microcrystals as a high performance psuedocapacitor electrode. *J. Alloys Compd.* **2016**, *656*, 707−713.
(58) Goda, E. S.; Pandit, B.; Hong, S. E.; Singu, B. S.; Kim, S. K.; Moustafa, E. B.; Yoon, K. R. Zeolitic imidazolate framework-67 derived Al-Co-S hierarchical sheets bridged by nitrogen-doped graphene: Incorporation of PANI derived carbon nanorods for solid-state asymmetric supercapacitors. *J. Energy Chem.* **2022**, *74*, 429−445.
(59) Wang, W.; Wei, X.; Choi, D.; Lu, X.; Yang, G.; Sun, C. Electrochemical Cells for Medium- and Large-Scale Energy Storage: Fundamentals. In *Advances in Batteries for Medium and Large-Scale Energy Storage*; Menictas, C.; Skyllas-Kazacos, M.; Lim, T. M., Eds.; Woodhead Publishing, 2015, Chapter 1, pp 3−28.
(60) Wu, Q.; He, T.; Zhang, Y.; Zhang, J.; Wang, Z.; Liu, Y.; Zhao, L.; Wu, Y.; Ran, F. Cyclic stability of supercapacitors: materials, energy storage mechanism, test methods, and device. *J. Mater. Chem. A* **2021**, *9* (43), 24094−24147.
(61) Xu, Y.; Wei, J.; Tan, L.; Yu, J.; Chen, Y. A facile approach to $NiCoO_2$ intimately standing on nitrogen doped graphene sheets by one-step hydrothermal synthesis for supercapacitors. *J. Mater. Chem. A* **2015**, *3* (13), 7121−7131.
(62) Wei, Z.; Guo, J.; Qu, M.; Guo, Z.; Zhang, H. Honeycombed-like nanosheet array composite $NiCo_2O_4$/rGO for efficient methanol electrooxidation and supercapacitors. *Electrochim. Acta* **2020**, *362*, No. 137145.
(63) Sandhiya, S.; Sujithkrishnan, E.; Halder, B.; Hussain, S.; Elumalai, P. Tunable capacitive charge storage of NiCoLDH@rGO for high-energy capacitor: Performance of flexible solid-state capacitor. *J. Energy Storage* **2024**, *79*, No. 110117.
(64) Xu, Y.; Wang, L.; Cao, P.; Cai, C.; Fu, Y.; Ma, X. Mesoporous composite nickel cobalt oxide/graphene oxide synthesized via a

https://doi.org/10.1021/acsomega.4c10988
ACS Omega 2025, 10, 16457−16471

template-assistant co-precipitation route as electrode material for supercapacitors. *J. Power Sources* **2016**, *306*, 742−752.
(65) Gómez-Aguilar, J. F.; Escalante-Martínez, J. E.; Calderón-Ramón, C.; Morales-Mendoza, L. J.; Benavidez-Cruz, M.; Gonzalez-Lee, M. Equivalent circuits applied in electrochemical impedance spectroscopy and fractional derivatives with and without singular kernel. *Adv. Math. Phys.* **2016**, *2016*, No. 9720181.
(66) Qiao, Y.; Zhang, C.; Kong, F.; Zhao, Q.; Kong, A.; Shan, Y. Activated biochar derived from peanut shells as the electrode materials with excellent performance in Zinc-air battery and supercapacitance. *Waste Manage.* **2021**, *125*, 257−267.
(67) Zheng, Y.; Li, Z.; Xu, J.; Wang, T.; Liu, X.; Duan, X.; Ma, Y.; Zhou, Y.; Pei, C. Multi-channeled hierarchical porous carbon incorporated Co_3O_4 nanopillar arrays as 3D binder-free electrode for high performance supercapacitors. *Nano Energy* **2016**, *20*, 94−107.
(68) Tang, P.-Y.; Han, L.-J.; Genç, A.; He, Y.-M.; Zhang, X.; Zhang, L.; Galán-Mascarós, J. R.; Morante, J. R.; Arbiol, J. Synergistic effects in 3D honeycomb-like hematite nanoflakes/branched polypyrrole nanoleaves heterostructures as high-performance negative electrodes for asymmetric supercapacitors. *Nano Energy* **2016**, *22*, 189−201.
(69) Du, C.; Pan, N. High power density supercapacitor electrodes of carbon nanotube films by electrophoretic deposition. *Nanotechnology* **2006**, *17* (21), No. 5314.
(70) Al Kiey, S. A.; Hasanin, M. S. Green and facile synthesis of nickel oxide-porous carbon composite as improved electrochemical electrodes for supercapacitor application from banana peel waste. *Environ. Sci. Pollut. Res.* **2021**, *28* (47), 66888−66900.

https://doi.org/10.1021/acsomega.4c10988
ACS Omega 2025, 10, 16457−16471